Journal of
Ship&Ocean
Technology
©SEPTEMBER 2006

SOTECH Vol. 10, No. 3, pp. 1 ~ 16, 2006

Development of Viscous Boundary Conditions in an Immersed Cartesian Grid Framework

Jae-Doo Lee[1]

[1] Samsung Heavy Industries Co., Ltd., Daejon, Korea
Corresponding Author: jaedoo.lee@samsung.com

Abstract

Despite the high cost of memory and CPU time required to resolve the boundary layer, a viscous unstructured grid solver has many advantages over a structured grid solver such as the convenience in automated grid generation and vortex capturing by solution adaption. In present study, an unstructured Cartesian grid solver is developed on the basis of the existing Euler solver, NASCART-GT. Instead of cut-cell approach, immersed boundary approach is applied with ghost cell boundary condition, which can be easily applied to a moving grid solver. The standard k-ε model by Launder and Spalding is employed for the turbulence modeling, and a new wall function approach is devised for the unstructured Cartesian grid solver. Developed approach is validated and the efficiency of the developed boundary condition is tested in 2-D flow field around a flat plate, NACA0012 airfoil, and axisymmetric hemispheroid.

Keywords: unstructured grid, cartesian grid, immersed cell, viscous solver, RANS, wall function, solution adaption

1 Introduction

Unstructured grid methods can easily employ automated grid generation for complex geometries and solution adaption for vortex capturing. In spite of these advantages of the unstructured grid topology over the structured grid, until recently it could not be used for a viscous flow calculation due to the high cost of memory and CPU time to resolve the boundary layer. As high performance parallel computer systems have become more recently available, the unstructured grid solvers have been very popular even in the calculation of viscous and turbulent flow.

Many unstructured grid solvers use pyramid or prism type grid topology, in which the cells are body-fitted and it is easy to apply conservative integration for finite volume method. However, the numerical solution of the equations of fluid dynamics is simplified and the truncation error would be greatly reduced, if the discretization is performed in a Cartesian coordinate system. Many flow simulations involve complex geometries with curved and planar boundaries oblique to the grid. For an accurate simulation, the computational domain of Cartesian grid solver should include arbitrary cut cell near the solid. A common problem with cut cell is the creation of very small cells. This leads to problems with stiffness of the equations and non-physical fluctuations of flow variables near the body. In case of time-dependent simulations, it limits the time step and influences

the stability. Researchers have dealt with this in a number of ways, including hybrid grid (Charlton 1997), merged cell approach (Udaykumar 1997, 2001), and embedded cell method (Marshall 2002).

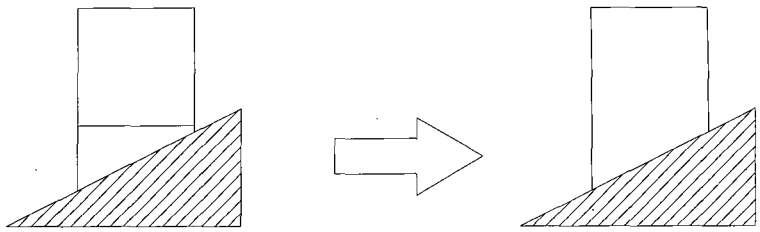

Figure 1: Illustration of merged cell approach

The hybrid grid topology employs the body-fitted structured grid near wall combined with Cartesian grid away from body. Using the structured grid near wall, however, the laborious grid generation and complicated coordinate transformation are still required. Merged cell approach uses a Cartesian grid for all cells except those which are intersected by the boundary in Figure 1. The boundary cells are truncated and merged into a nearest flow cell so that they conform to the shape of the boundary surface. Since the flow properties at the merged cell center are integrated from the wall boundary and flow cells, the state vector is always conservative. However, it generally entails a considerable increase in complexity, since fluxes between diagonally adjacent cells must also be calculated, and the computational molecule for merged boundary cells become different to that used for the standard cells. Since the merged cell center is not aligned with other flow cells, the order of accuracy in spatial discretization is limited during integration of flow cells contacting the merged cell. Embedded boundary method is to remove the surface cells from the finite volume formulation and extrapolate flow properties on the boundary cell center from a reference point. However, it is still required in an embedded boundary cell method to relocate the cell center to the centroid of the truncated cell as shown in Figure 2.

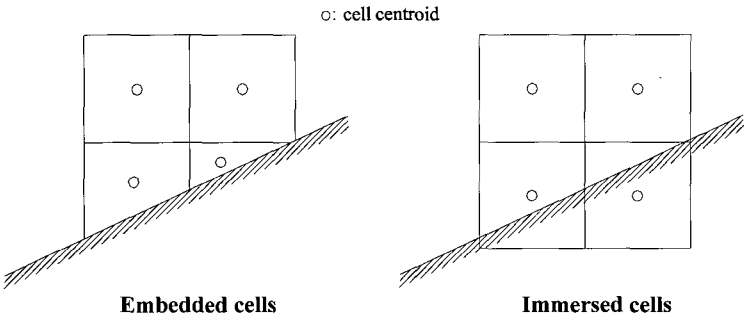

Figure 2: Comparison of embedded and immersed cells

The immersed boundary method using ghost cell was first introduced by Forrer and Jeltsch (1998) for Cartesian grid. The boundary cell is not truncated and maintains cubic shape. As shown in Figure 2, the boundary cell center is not shifted to the cut-cell center and maintains at the centroid of non-cut cell independent of boundary shape. Dadone

(2002) successfully solved the 2D and 3D Euler equation for an unstructured Cartesian grid using the ghost-cell immersed boundary method. He considered solid walls as boundaries immersed in the flow field and enforced boundary conditions at ghost cell centers located inside the body in a position close to the wall. It solved the problem of the misalignment of cell centers. It also eliminated the requirement of finding cell centroids thereby saving computer memory.

To date, most unstructured Cartesian grid techniques have been developed to solve the Euler equations. Excluding the hybrid grid solver, there has been relatively little research for the full Navier-Stokes or RANS equations. Furthermore, no viscous modeling using an immersed cell approach has been reported yet. It is quite challenging and has never done before to apply wall function approach to immersed Cartesian grid. The difficulty lies in the inability to acquire smooth variation of y^+ in the desired range due to the non-body-fitted cells near the solid wall. Applying the conventional wall function wall boundary condition on the immersed Cartesian cells near the wall would result in a large magnitude of non-physical fluctuations of the flow properties, thereby, cause instability of the computation. The wall function boundary condition developed in this work yields stable and reasonable solution within the accuracy of the turbulence model. The grid efficiency is also improved with respect to the conventional method by extending the first cell center from the wall boundary up to $y^+ \approx 300$.

2 Numerical Flow Solver

NASCART-GT (Numerical Aerodynamic Simulation via CARTesian Grid Technique) is a compressible, unsteady, three-dimensional Cartesian grid solver of the RANS (Reynolds Averaged Navier-Stokes) equation set, which assumes calorically perfect gas. The molecular viscosity is calculated from Sutherland's law. The RANS equations are solved using Roe's approximate Riemann solvers coupled with a MUSCL scheme for inviscid fluxes and traditional finite differencing of the viscous terms. The primitive variables at the hanging node are interpolated using 2^{nd} order pseudo-Laplacian averaging scheme. For turbulent flow simulation, the standard k-ε model by Launder and Spalding (1974) is employed. The time integration is performed using a Hancock two-stage scheme which is second order accurate in time. To ensure the positivity of turbulent quantities, a turbulent limiter is applied derived from the asymptotic analysis of k and ε equations. Solution adaption is performed at user-specified iteration numbers based on divergence, vorticity, turbulent kinetic energy and dissipation rate. For more detail, see the author's thesis (Lee 2006). The following sections explain boundary conditions in detail.

2.1 Laminar wall boundary conditions

Instead of directly specifying boundary conditions on a wall, NASCART-GT enforces primitive variables on the ghost cells such as 15 and 16 in Figure 3, which act as wall boundaries. The state vector of cells intersected by the solid wall (called boundary cell, for example, 11, 12 and 14 in Figure **3**) are found using time integration as the same manner with flow cells. The point B and D represent the reference points of cell 16 and 15 respectively. The location of reference point is determined as following. First, find the closest point on a body panel from the ghost cell center, i.e. point A or C. Then, extend the line connecting the ghost cell center and the closest point on the wall panel to the extent of predetermined length, δ_r. In current study, δ_r is set to the length of boundary cell diagonal. The primitive variables at a reference point are interpolated from the primitive

variables of the 3 closest neighbor cell centers using the linear least square interpolation. After finding primitive variables at the reference point, the variables at the ghost cell center are calculated using linear extrapolation.

For pressure, the condition $\partial p / \partial \eta = 0$ is satisfied by setting the pressures on the wall and the ghost cell center are identical to that at the reference point, i.e. $p_{ref} = p_w = p_g$, where η is local coordinate normal to the wall and the subscripts ref, w and g denote reference point, wall and ghost cell center, respectively. Adiabatic wall boundary condition is fulfilled when $\partial T / \partial \eta = 0$ is enforced as the same manner with the pressure boundary condition. To find the velocity components at the ghost cell center, the velocity at the reference point is transformed to get the tangential and normal velocities.

$$\boldsymbol{V}_{N,ref} = (\boldsymbol{V}_{ref} \cdot \boldsymbol{n})\boldsymbol{n} \tag{1}$$

$$\boldsymbol{V}_{T,ref} = \boldsymbol{V}_{ref} - \boldsymbol{V}_{N,ref} \tag{2}$$

where the subscripts N and T represent normal and tangential components, respectively. $\boldsymbol{n}$ is unit normal vector of the surface panel. Normal velocity on the wall should be zero in a non-permeable wall. Thus, linear extrapolation results in

$$\boldsymbol{V}_{N,g} = -\frac{\delta_g}{\delta_r}\boldsymbol{V}_{N,ref} \tag{3}$$

No slip condition for a laminar wall is enforced, such that the tangential velocity is

$$\boldsymbol{V}_{T,g} = -\frac{\delta_g}{\delta_r}\boldsymbol{V}_{T,ref} \tag{4}$$

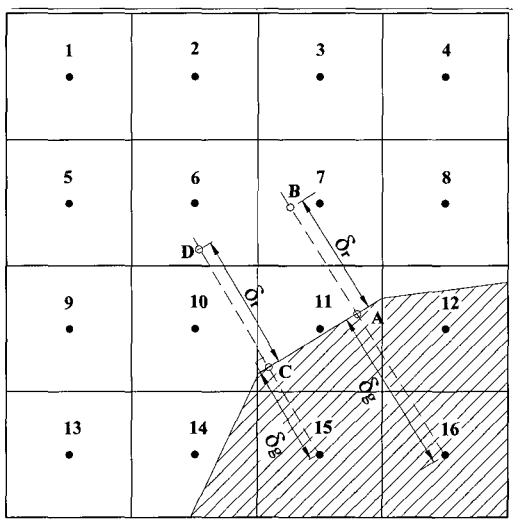

Figure 3: Example configuration of wall boundary treatment

2.2 Wall function approach

NASCART-GT employs the Spalding's formulation, which yields a unified form valid for the log law layer and the viscous sublayer as well as the buffer layer. It is known that the Spalding's formulation shows excellent agreement with various experimental data even after, for $y^+ > 300$, the outer law commences (White 1991).

$$y^+ = u^+ + e^{-\kappa B}\left[e^{\kappa u^+} - 1 - \kappa u^+ - \frac{(\kappa u^+)^2}{2} - \frac{(\kappa u^+)^3}{6}\right] \tag{5}$$

For the given temperature and tangential velocity at the reference point, the adiabatic wall temperature is calculated from the Crocco-Busemann equation.

$$T_w = T_{ref} + \frac{r}{2}\frac{V_{T,ref}^2}{c_p} \tag{6}$$

where r is the recovery factor known to be $\mathrm{Pr}^{1/3}$ in turbulent flows for air. c_p represents the specific heat. The wall density is obtained from the state law for calculated wall temperature and wall pressure that is equal to the reference point pressure. Then, the wall shear stress at the reference point can be calculated by solving equation (5) numerically, i.e. Newton's method.

The next step is to implement the computed wall shear stress into the governing equations. With coarse grid spacing near wall, incorrect velocity gradient and wall shear stress will be obtained when no-slip condition is applied. One approach to introducing the wall function corrected wall shear stress into the calculation of the viscous flux is to calculate the effective turbulent viscosity so that the discrete shear stress at the boundary cell face yields the correct value for the wall shear stress (Chitsomboon 1995). Unfortunately, this method may results in errors into the energy equation if a separate effective turbulent viscosity for the temperature is not used.

Instead of modifying turbulent viscosity, calculated shear stress by wall function can be directly imposed on the face near wall. Sondak and Pletcher (1995) introduced a procedure to perform a transformation of the stresses for generalized coordinate system with body-fitted structured grid. He used the standard tensor transformation to get

$$\tau_{\alpha\beta} = \frac{\partial \xi_\alpha}{\partial x_i}\frac{\partial \xi_\beta}{\partial x_j}\tau_{ij} \tag{7}$$

where α and β represent the geodesic coordinate, and i and j the Cartesian coordinate. As seen, the above method needs very complicated coordinate transformation, which would increase truncation error and emasculate the advantage of the Cartesian grid. To make the matters worse, non-physical fluctuations of primitive variables are induced when Sondak's method is combined with the staggered Cartesian grid. The fluctuations may result in fictitious separation and distort the whole solution. This is mainly caused by the opposite directional velocity of the cells whose center is located inside of the wall. The nonlinear velocity profile combined with sharp change in the distances from the cell center to the wall induces the non-physical fluctuations.

To solve previously stated problems, a new wall function boundary condition is devised in the present study. It is based on the idea that the modified tangential velocity satisfying discrete wall shear stress approximation would eliminate the use of the complicated coordinate transformation. This makes the computational cells near wall to remain in numerically linear region, thereby, the computation would be stable. The approach is described in the following.

The normal velocity is specified by the equation (3) to ensure zero normal velocity on the wall. Since the total wall shear stress near the wall is approximately constant, the wall shear stress at the ghost cell is set to be the same as that at the reference point. Assuming the total viscosity (the sum of molecular viscosity and eddy viscosity) of the ghost cell is identical to that of the reference point, the shear stress in the solver is approximated as

$$\tau_w \approx \left(\mu_{l,ref} + \mu_{t,ref}\right)\frac{\Delta V_T}{\Delta \eta} = \left(\mu_{l,ref} + \mu_{t,ref}\right)\frac{V_{T,ref} - V_{T,g}}{\delta_r - \delta_g} \tag{8}$$

Then, the tangential velocity of the ghost cell is

$$V_{T,g} \approx V_{T,ref} - \frac{\delta_r - \delta_g}{\mu_{l,ref} + \mu_{t,ref}}\tau_w \tag{9}$$

Applying linear tangential velocity at the ghost cells may result in non-physical mean velocity at boundary cells. However, this condition satisfies the required wall boundary conditions of zero normal flux and wall shear stress, and the flow cells outside of the boundary cells would have proper values. The pressure boundary condition is in the same manner with the laminar wall conditions. The temperature of the ghost cell follows the Crocco-Busemann relation from the reference point temperature and computed tangential velocity. This is based on the fact that the adiabatic wall temperature is constant along the normal ray near wall.

$$T_g = T_{ref} + \frac{r}{2}\frac{V_{T,ref}^2 - V_{T,g}^2}{c_p} \tag{10}$$

The density is obtained from the state law. The remaining step is to find the boundary conditions for turbulent properties, k and ε. The boundary conditions of k and ε have to satisfy the assumption of the equation (8). At the same time, the eddy viscosity should follow the designated profile, which is described in the reference (Nichols and Nelson 2004).

$$\frac{\mu_t}{\mu_l} = \kappa e^{-\kappa B}\left[e^{\kappa u^+} - 1 - \kappa u^+ - \frac{\left(\kappa u^+\right)^2}{2}\right] \tag{11}$$

To fulfill these requirements, the boundary conditions for turbulent properties are imposed on the flow cells contacting the boundary cells, as well as the ghost cells and boundary cells. Figure 3 shows the example of the flow cells (e.g. the cells 6~9, and 13), on which the turbulent boundary conditions are enforced. Assuming that the shear stress is constant near the wall, the turbulent kinetic energy at the cell center is equal to

$$k = \frac{u_\tau^2}{\sqrt{C_\mu}} \tag{12}$$

Given the eddy viscosity from the equation (11), the dissipation rate of the turbulence energy is set to satisfy the turbulent viscosity according to the Launder and Spalding's turbulence model.

$$\varepsilon = C_\mu \rho \frac{k^2}{\mu_t} \tag{13}$$

For boundary cells and ghost cells, the turbulent properties are specified using the reference point properties. The constant total viscosity condition along the ray yields to

$$\mu_t = \mu_{l,ref} + \mu_{l,ref} - \mu_l \tag{14}$$

The turbulent kinetic energy and dissipation rate are specified using the equations (12) and (13), respectively.

2.3 Inflow and outflow boundary conditions

For outflow and inflow boundaries, characteristic boundary condition or simple extrapolation is applied to specify Riemann invariants. For turbulent flow calculation, the turbulent kinetic energy and dissipation rate are assumed to be known at the inlet boundary from the prescribed turbulence intensity and the turbulent viscosity. A value for the ratio of freestream turbulent viscosity to laminar viscosity is also specified, such that

$$k_\infty = I_t V_\infty \tag{15}$$

$$\mu_{t,\infty} = C_1 \mu_\infty \tag{16}$$

The resultant freestream turbulent dissipation is obtained from turbulent viscosity closure. I_t represents turbulent intensity and generally set to 0.01 for external flows. Improper value of C_1 may result in slow convergence. In NASCART-GT, it is set to 0.1 (Hunt and May 1999). Limiting the values of k and ε of the flow cell to the freestream values after each time step, helps prevent unphysical transient solution (Sondak and Pletcher 1995). At the outflow boundary, k and ε are extrapolated according to the characteristic boundary condition.

3 Validations

The validation of the developed numerical approach is performed on the various 2-D viscous flows including the laminar and turbulent flows over flat plate and NACA 0012 airfoil, and the axisymmetric turbulent flow over a hemispheroid. The results are compared with analytical solution or experimental data. All the results shown in this chapter are obtained using the 3rd order interpolation of the inviscid fluxes.

3.1 Flat plate

A body-aligned Cartesian grid is generated to calculate turbulent flow over a two-dimensional flat plate. Inflow boundary is located ahead of the leading edge, and outflow boundary is on the trailing edge. On the inflow boundary, the characteristic boundary condition is enforced as usual. On the upper and outflow boundaries, however, the primitive variables are extrapolated instead of characteristic boundary condition to ensure the flow smoothly sweep out. In both laminar and turbulent calculations, the freestream Mach number is set to 0.2 to avoid incompressible limit of the solver.

Laminar Flow

The Reynolds number is set to 20,000 based on the chord length. The vertical computational boundaries are the trailing edge and one chord ahead of the leading edge, in which the square root cells of 16×4 are generated and 8 level of grid refinement is performed. In Figure 4 and Figure 5, the computed skin friction coefficient and the velocity profile at half-chord are presented. They show good agreement with analytical Blasius solution. The computed boundary layer thickness is also compared very well with the analytical solution.

Turbulent Flow

The Reynolds number based on flat plate length is 1.0927×10^7, at which the skin friction and velocity profiles have been measured by Wieghardt (1951). The computational domain and root cell dimension are identical to the laminar calculation. However, the grid is finer than the laminar case such that the maximum grid refinement levels are 8 for coarse grid and 9 for fine grid. This results in the largest y^+'s of 384.6 and 210.1, respectively, based on the reference point, which are larger than the cell size requirement of most RANS solvers. The surface roughness parameter was not measured, either. A value of $B = 5.0$ was used in the law of the wall assuming smooth wall.

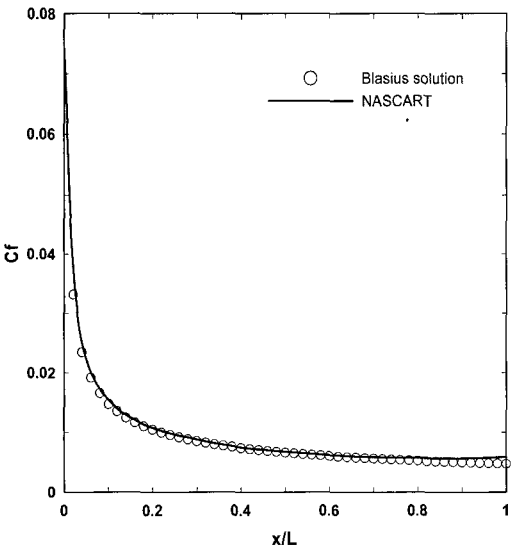

Figure 4: Computed C_f over laminar flat plate

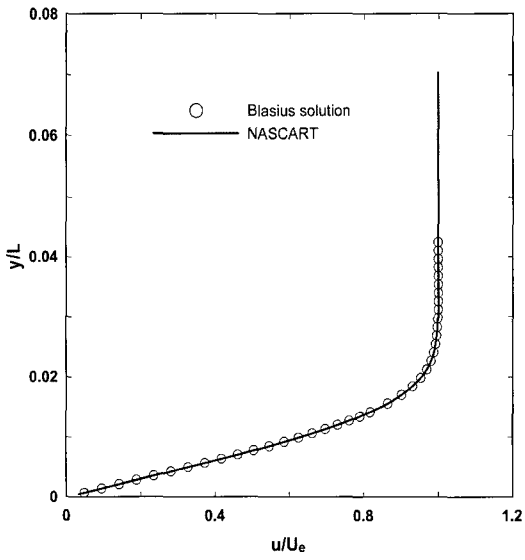

Figure 5: Laminar velocity profile at half chord

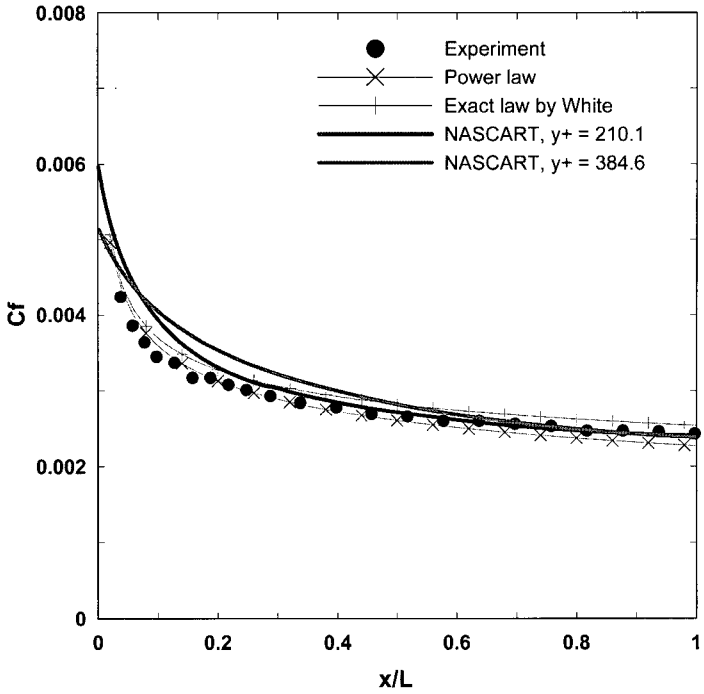

Figure 6: Computed C_f over turbulent flat plate

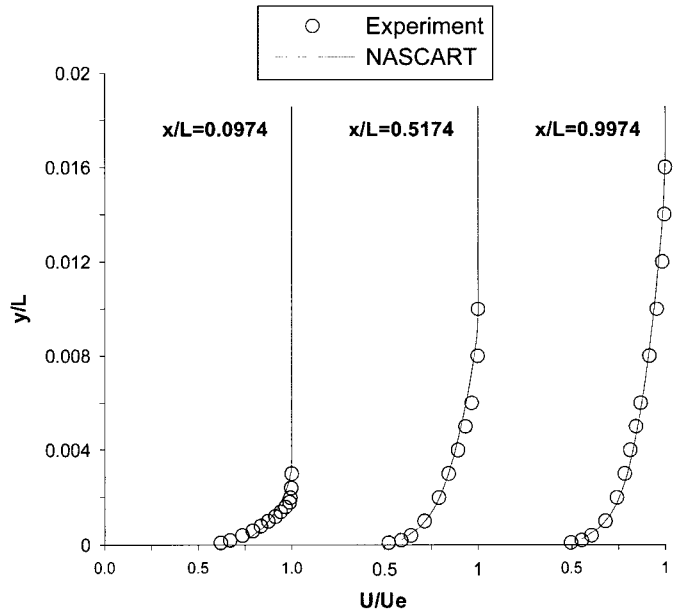

Figure 7: Mean velocity profiles on turbulent flat plate

The computed skin friction is compared with the power law, exact law by White (1991), and the experiments in Figure 6. Aft of the mid-chord, the measured skin friction is between the power law and the exact law, which is well analyzed by NASCART. As shown in the picture, the skin friction changes rapidly near the leading edge. The inaccuracy of the computed skin friction near the leading edge might be caused by the

insufficient local grid resolution. It is easily noted that the difference between the results of the computations and experiments near the leading edge is decreased as the y^+ decreases. It is expected that the computed skin friction will further approach to the experimental data with higher grid resolution. In spite of the small error near the leading edge caused by insufficient grid resolution, the solution with the coarse grid shows good agreement with the results of fine grid computation and experiment at the trailing edge.
Figure 7 shows the comparison of computed with fine grid and measured mean velocity profile at various locations. It is observed that the calculated mean velocity profile and boundary layer thickness have good correlation with the measurements. Slight over-prediction of the boundary layer thickness from station 1 thru 4 is also induced by the insufficiently large cells, which smears out the high velocity gradient.

3.2 NACA 0012 Airfoil

Laminar flow

The freestream Mach number is 0.8 and the angle of attack is 10 degree. Reynolds number based on chord length is 500. Since there is no experimental data available in such a low Reynolds number, the computed results are compared with the solution of verified multi-grid solver by Casalini (1999). Marshall (2002) also performed the former version of NASCART calculation on the same flow condition. Marshall employed the embedded Cartesian grid method in which the primitive variables at the cut-cell centroid are extrapolated from the reference point instead of using ghost cell.

The computational boundaries are 5 chords ahead of and behind the airfoil, above and below the airfoil centerline. The root grid dimension is 33×30, and 6 level of refinement is applied for the coarse grid. The computational cells of the coarse grid calculation are identical to those of Marshall's calculation. For the fine grid case, 8 level of refinement is employed with the root grid dimension of 22×20. The solution adaption is performed based on divergence and vorticity.

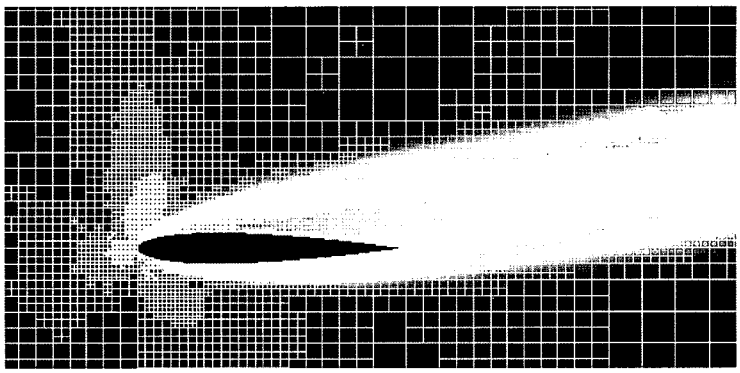

Figure 8: Final grid configuration and entropy contours around transonic NACA 0012 airfoil

Figure 8 shows the final grid configuration and entropy contours after solution adaption. The grids are refined near the stagnation point and in the shock pocket due to the large divergence variation. The cells are also refined inside the boundary layer and wake region where the high vorticity appears. The computed distributions of Cp and Cf with coarse grid are presented in Figure 9 and Figure 10. In Figure 10, negative skin friction does not mean a separated flow, but is instead used to denote skin friction in the lower surface of the airfoil. The solution of current NASCART has better accuracy than Marshall's results in the prediction of the stagnation pressure and suction peak in Figure 9. The computed skin

friction also shows better agreement with the reference data. With respect to the unphysical fluctuations, the present results give smoother variation than the Marshall's in both of pressure and skin friction. The improvement is the result of the use of the conservative ghost cell approach and coordinate-aligned cell centers in the new version of NASCART. The under-estimations of suction peak pressure and skin friction near the leading edge can be solved by increasing grid resolution as shown in Figure 11 and Figure 12. The computed Cp's and Cf's are compared well with the reference data.

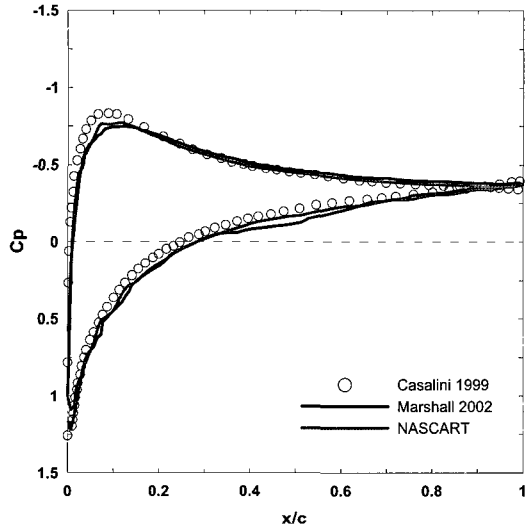

Figure 9: Pressure distribution over transonic NACA 0012 airfoil with coarse grid

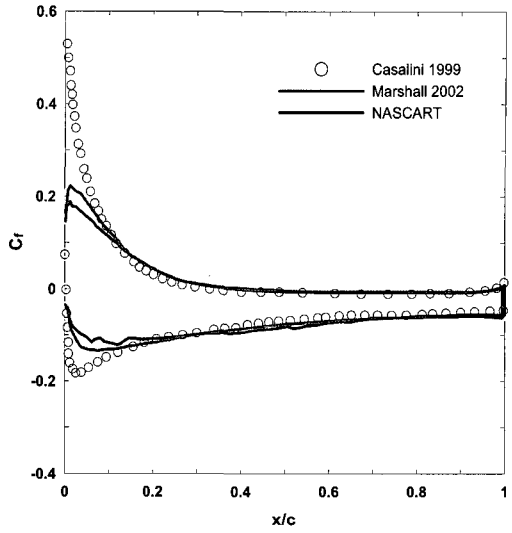

Figure 10: Skin friction distribution over transonic NACA 0012 airfoil with coarse grid

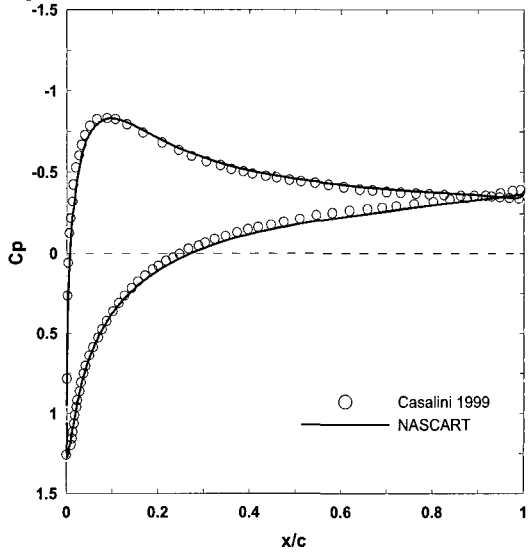

Figure 11: Pressure distribution over transonic NACA 0012 airfoil with fine grid

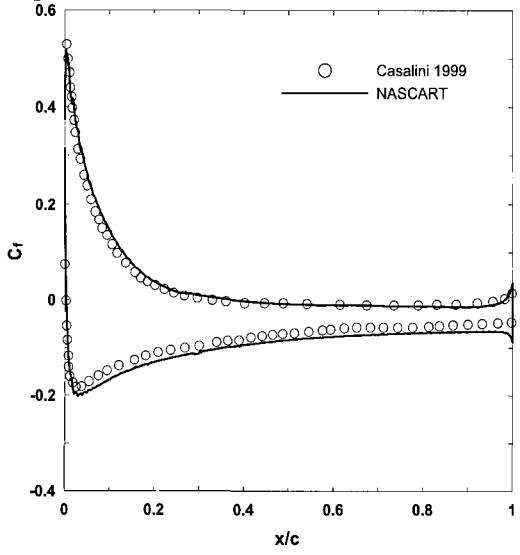

Figure 12: Skin friction distribution over transonic NACA 0012 airfoil with fine grid

Turbulent flow

Turbulent modeling is tested over a NACA0012 airfoil at a Mach number of 0.3, a chord Reynolds number of 1.86 million, and an incidence of 3.59 degrees. The computational boundaries are the same as the laminar calculation. The root grid dimension is 22×20 and 8, 9 and 10 levels of refinement are applied to get the maximum y^+ based on the reference point of 81.1 up to 287.2. The characteristic boundary conditions are applied on the inflow and outflow boundaries. A smooth wall is assumed to specify $B = 5.0$ for the law of the wall. The computed pressure coefficients are compared with AGARD experimental data in Figure 13, and very good correlations are observed even with very coarse grid of y^+=287.2.

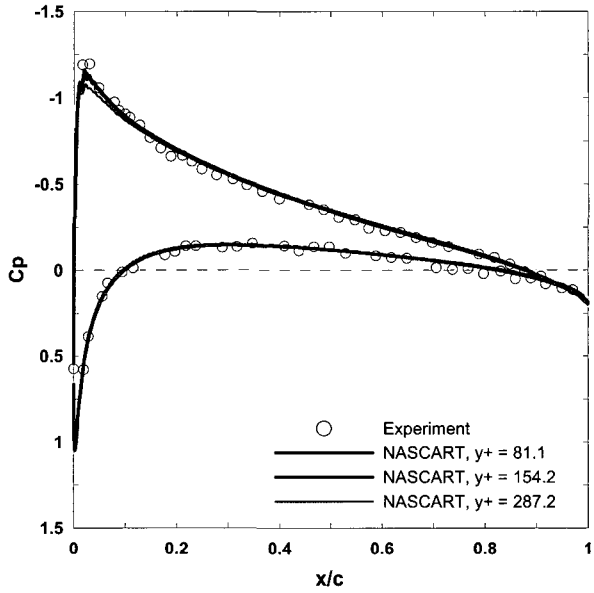

Figure 13: Pressure coefficients with various cell sizes over turbulent NACA 0012 airfoil

Table 1: Effect of cell size on accuracy and computational cost for NACA 0012 airfoil calculations

Grid density		Fine	Medium	Coarse
Accuracy	c_l	0.3584	0.3583	0.3489
	$^{+}$Error (%)	0.1671	0.1950	2.813
Computer memory	No. of cells	72,520	37,672	20,176
	$^{++}$Saving (%)	N/A	48.1	72.2
Computation time	* CPU time (hr)	44.7	16.9	3.1
	$^{++}$Saving (%)	N/A	62.2	93.1

$^{+}$ Based on the airfoil data of $c_l = 0.3590$

$^{++}$ Based on the RANS fine grid calculation

* CPU time is obtained using Pentium IV 2.4 GHz PC

For the quantitative analysis of the grid efficiency, the effects of the cell sizes on the accuracy and computational cost from the solutions of NACA 0012 airfoil flows are presented in Table 1. Errors are calculated based on the airfoil data (Abbott and Von Doenhoff 1959) and the savings on the solutions of the RANS with the fine grid. There is little difference between computed lift coefficients for fine and medium grids whose errors are less than 0.2 %. Meanwhile the savings of computer memory and computation time are observed by over 48 % and 62 %, respectively. As mentioned before, conventional wall function approach requires small cells near wall to yield $y^+<80$ for proper turbulence modeling. This demonstrates the fact that the developed wall function approach has better grid efficiency and computational time than the conventional methods. Considering the coarse grid case, the accuracy is deteriorated just by 2.813 % while the computational time is improved by over 93 % with respect to the fine grid solution and over 81 % to the medium grid solution. It is, therefore, apparent that the implementation of coarse grid with the developed wall function method is practical and efficient approach in the overall prediction of the aerodynamic forces, yielding reasonable solution within the accuracy of the present turbulence model.

3.3 Axisymmetric Hemispheroid

The turbulent boundary layer on the hemispheroid was measured by Ramaprian et al. (1981) to provide validation data for computational development. The model configuration combines a hemispherical nose with a hemispheroidal rear. The experiments are performed at the Reynolds number (based on the length of the body) of 2.0×10^6. The nominal wind-tunnel velocity is 22.0 $m/\sec$ thereby $M_\infty \approx 0.063$. The computational Mach number is increased to avoid the incompressible limit of the code, and the computations are performed for axisymmetric flow. The velocity profile and skin friction are measured at 8 traverse stations, which are shown in the reference. The computational boundaries are 5 times body length ahead of and behind the hemispheroid, above and below the centerline. The root grid dimension is 28×24, and 8, 9, and 11 levels of refinement are applied. The freestream Mach number is increased to 0.3 to prevent poor conditioning of the compressible flow solver. The constant related to the roughness parameter is set to $B = 5.5$ according to the experiments.

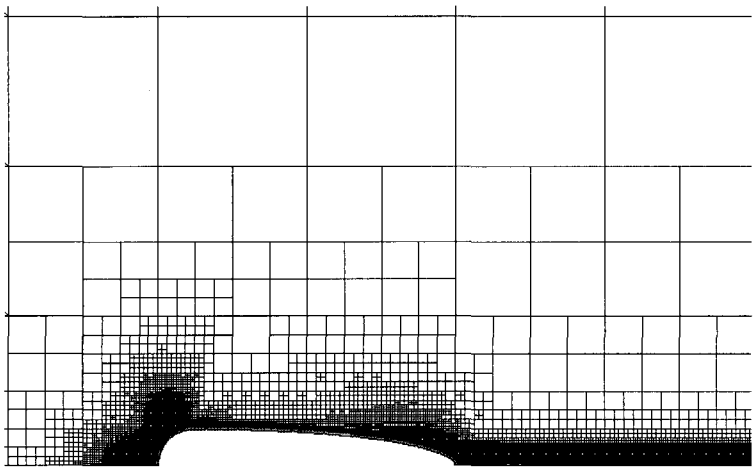

Figure 14: Final grid configuration over axisymmetric hemispheroid

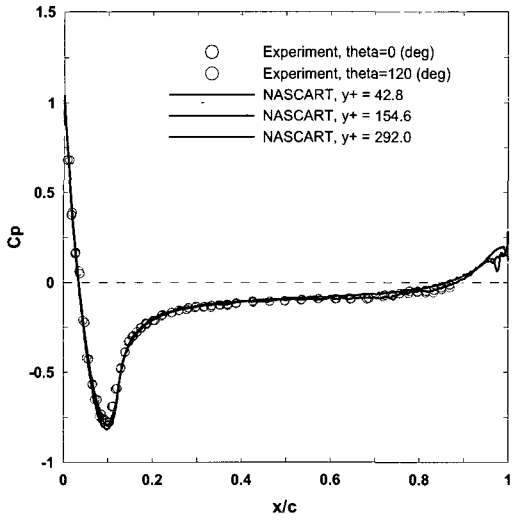

Figure 15: Pressure coefficients with various cell sizes over hemispheroid

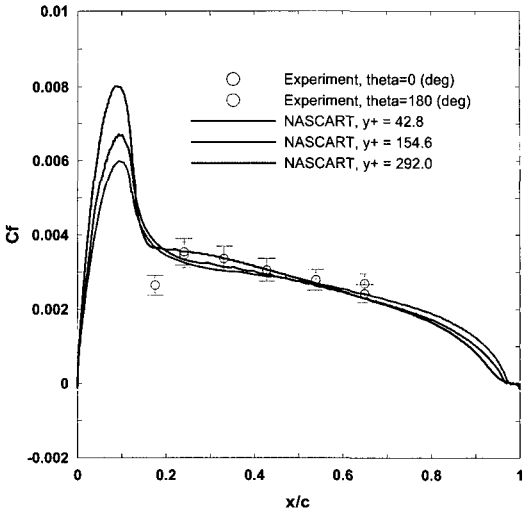

Figure 16: Skin friction coefficients with various cell sizes over hemispheroid

Figure 14 shows the final grid configuration, in which the red line represents the wall boundary. The cells are refined near the leading edge and wake region where the large gradients of divergence and vorticity exist. The computed pressure distributions are shown in Figure 15, compared with the experimental data. The pressures are measured at circumferential angles of 0 and 120 degrees. The difference between the measured pressures is very small, and the computational results show very good agreement with them even with $y^+ \approx 300$. In Figure 16, calculated skin frictions are compared with the experiments, in which the skin frictions are measured at the circumferential angles of 0 and 180 degrees. Since the flow is axisymmetric, the difference between these two is considered as an experimental error. According to the reference paper, the estimated error of the instrument in the wall shear stress measurement is 5 %. It is, however, reported that a considerable uncertainty exists due to the deviation of the angle between the velocity vector and the probe axis. Therefore, the error of the measured skin friction is assumed to be 10 % that corresponds to the difference of skin friction coefficients at station 6. The results of NASCART are well correlated to the experiment within the estimated error with the exception of the first measurement station. At station 1, the computed skin friction is overestimated, which also has been observed by Sondak and Pletcher (1995). They computed the turbulent flow over the same hemispheroid using three turbulence models (Baldwin-Lomax algebraic model, Launder and Spalding $k-\varepsilon$ model, and Chien's low Reynolds number $k-\varepsilon$ model), and none of the models predicts the proper skin friction at station1. This discrepancy would be caused by the transition from laminar to turbulent flows in the experiment, which is not modeled in numerical analysis. This would explain the fact that the measured skin friction coefficient is lower than the computed values and that the computation over-predicts the tangential velocity at station 1 in the subsequent plot. The computed velocity distributions with fine grid are presented in Figure 17, and the results compare reasonably well with the test data.

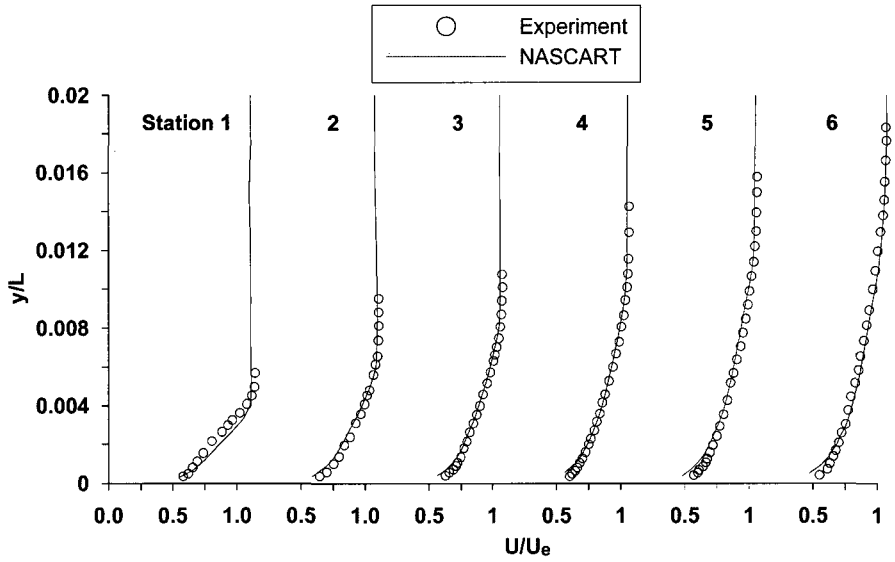

Figure 17: Comparison of mean velocity profiles in flow field around hemispheroid

4 Conclusions

In present study, new viscous wall boundary conditions are implemented into the existing unstructured Cartesian grid framework. A number of conclusions are shown below.

- The boundary cell centroids aligned with the flow cell centers make the numerical stencil orthogonal and reduce the error in the volume integration. The application of ghost cell approach also increases the accuracy by the use of conservative volume integration in the calculation of boundary cells just like in flow cell calculation instead of simple extrapolation of the flow properties. This yields an accurate prediction of skin friction and velocity profile in a boundary layer as well as the pressure.

- The new boundary condition is developed and successfully tested for an immersed Cartesian grid viscous solver, which is never done before. The developed wall function approach yields stable and reasonable solution within the accuracy of the turbulence model. The new approach removes the complicated coordinate transformation required in the conventional wall function approach.

- Unlike the conventional wall function approach, the developed method shows stable and reasonable solution with a relatively coarse grid system within the accuracy of the turbulence model. The use of a coarse grid with the developed wall function approach can reduce the computational memory and computation time.

References

Experimental Data Base for Computer Program Assessment , AGARD Advisory Report No. 138.

Abbott, I.H. and A.E. Von Doenhoff. 1959. Theory of Wing Sections, Dover Ed.

Casalini, C. and A. Dadone. 1999. Computations of Viscous Flows Using a Multigrid Finite Volume Lamda Formulation, Engineering Computations, **16, 7,** 767-786.

Charlton, E.F. 1997. An Octree Solution to Conservation-laws over Arbitrary Regions(OSCAE) with Applications to Aircraft Aerodynamics, PhD Thesis, University of Michigan.

Chitsomboon, T. 1995. Improved Artificial Viscosity for High-Reynolds-Number k-ε Turbulence Model, AIAA Paper 95-2166.

Dadone, A. and B. Grossman. 2002. An Immersed Body Methodology for Inviscid Flows on Cartesian Grids, AIAA Paper 2002-1059.

Forrer, H. and R. Jeltsch. 1998. A Higher Order Boundary Treatment for Cartesian-Grid Method, Journal of Computational Physics, **140,** 259-277.

Hunt, D.L. and N.E. May. 1999. Practical Use of Transport Turbulence Models in Aerospace-CFD Implementation and Applications, AIAA Paper 99-3137.

Launder, B.E. and D.B. Spalding. 1974. The Numerical Computation of Turbulent Flows, Computer Methods in Applied Mechanics and Engineering, **3,** 269-289.

Lee, J.D. 2006. Development of an Efficient Viscous Approach in a Cartesian Grid Framework and Application to Rotor-Fuselage Interaction, PhD Thesis, Georgia Institute of Technology.

Marshall, D.D. 2002. Extending the Functionalities of Cartesian Grid Solvers: Viscous Effects Modeling and MPI Parallelization, PhD Thesis, Georgia Institute of Technology.

Nichols, R.H. and C.C. Nelson. 2004. Wall Function Boundary Conditions Including Heat Transfer and Compressibility, AIAA Journal, **42, 6,** 1107-1114.

Ramaprian, B.R., V.C. Patel. and D.H. Choi. 1981. Mean-Flow Measurements in the Three-Dimensional Boundary Layer over a Body of Revolution at Incidence, Journal of Fluid Mechanics, **103,** 479-504.

Sondak, D.L. and R.H. Pletcher. 1995. Applications of Wall Functions to Generalized Nonorthogonal Curvilinear Coordinate System, AIAA Journal, **33, 1**.

Udaykumar, H.S. 1997. Multiphase Dynamics in Arbitrary Geometries on Fixed Cartesian Grids, Journal of Computational Physics, **137, 2,** 366-405.

Udaykumar, H.S. 2001. A Sharp Interface Cartesian Grid Method for Simulating Flow with Complex Moving Boundaries, Journal of Computational Physics, **174,** 345-380.

White, F.M. 1991. Viscous Fluid Flow, 2nd Ed., McGraw-Hill.

Wieghardt, K. and W. Tillmann. 1951. On the Turbulent Friction Layer for Rising Pressure, NACA TM 1314.